

Topological Boundary Modes from Translational Deformations

Yosuke Nakata,^{1,2,*} Yoshitaka Ito,¹ Yasunobu Nakamura,^{1,3} and Ryuichi Shindou^{4,5}

¹Research Center for Advanced Science and Technology (RCAST),
The University of Tokyo, Meguro-ku, Tokyo 153-8904, Japan

²Graduate School of Engineering Science, Osaka University, Toyonaka, Osaka 560-8531, Japan

³Center for Emergent Matter Science (CEMS), RIKEN, Wako-shi, Saitama 351-0198, Japan

⁴International Center for Quantum Materials, Peking University, Beijing 100871, China

⁵Collaborative Innovation Center of Quantum Matter, Beijing 100871, China

(Dated: February 25, 2020)

Localized states universally appear when a periodic potential is perturbed by defects or terminated at its surface. In this Letter, we theoretically and experimentally demonstrate a mechanism that generates localized states through continuous translational deformations of periodic potentials. We provide a rigorous proof of the emergence of the localized states under the deformations. The mechanism is experimentally verified in microwave photonic crystals. We also demonstrate topological phase windings of reflected waves for translated photonic crystals.

In the 1930s, Tamm predicted the localized state of an electron near the surface of a solid [1]. Years later, Shockley proposed another mechanism that produces surface states, based on a band inversion of atomic orbitals [2]. Impurities and lattice defects inside a crystal also produce localized states [3, 4], which play important roles in doped semiconductors. While such localized states were first investigated for electrons, they universally appear in various wave systems. Zero-dimensional localized states have been observed in electronic superlattices [5], photonic and magnetophotonic crystals [6–8], plasmonic crystals [9–13], and phononic crystals [14].

The recent discovery of topological insulators has shed fresh light on the understanding of surface states in various wave systems from a topological perspective. Under time-reversal symmetry, bulk electronic states in band insulators are generally characterized by the Z_2 topological invariant [15, 16]. The bulk-edge correspondence relates the bulk Z_2 topological invariant to surface characteristics and ensures an existence of gapless boundary states with the Kramers degeneracy protected by time-reversal symmetry [17, 18]. Later, it was shown that other discrete symmetries and their combinations generate various topological numbers for bulk electronic states and associated in-gap gapless boundary states [19]. A pioneering example is the Z topological invariant with a sublattice symmetry in the Su-Schrieffer-Heeger model [20, 21]. The nonzero topological integer in the Su-Schrieffer-Heeger model ensures zero-energy end states with sublattice-symmetry protection. For continuous one-dimensional crystals with inversion symmetry, Xiao *et al.* established a relation between surface observables and bulk properties and rigorously determined the existence or nonexistence of localized states [22]. So far, research on one-dimensional systems has focused on unit cells with either sublattice or inversion symmetry to define the topological integers, but these discrete symmetries may not be essential, as suggested by Shockley [2]. In fact, the in-gap localized states as boundary states could survive under a

gradual structural deformation that breaks the symmetries within the unit cell. This consideration indicates an alternative topological mechanism that generates localized states without using any symmetry protection.

In this letter, we devise a scheme that produces zero-dimensional localized states in a defect created by a translational deformation of a periodic potential. A rigorous proof of emergence of the localized states is provided without relying on any symmetry protection. The scheme is experimentally demonstrated in microwave photonic crystals.

Consider a one-particle eigenmode in one-dimensional continuous media with a periodic potential of the period a . From the Bloch theorem [23], the eigenmode $|\psi_n(k)\rangle = \exp(ik\hat{x})|u_n(k)\rangle$ is characterized by the crystal momentum k in the first Brillouin zone $[-\pi/a, \pi/a]$ and the energy band index n , where $\langle x|u_n(k)\rangle$ is periodic in x . For simplicity, we assume that the eigenenergy $E_n(k)$ of $|\psi_n(k)\rangle$ satisfies $E_1(k) < E_2(k) < \dots$ in the entire Brillouin zone. From here, we focus on the n th band. The first Brillouin zone is discretized as $k_m = m\pi/(Ma)$ with $m = -M + 1, -M + 2, \dots, M$ ($2M$ points). In terms of $|u_m\rangle = |u_n(k_m)\rangle$, a Wilson loop is given by

$$W = \langle u_M|u_{M-1}\rangle \langle u_{M-1}|u_{M-2}\rangle \cdots \langle u_1|u_0\rangle \times \langle u_0|u_{-1}\rangle \cdots \langle u_{-M+2}|u_{-M+1}\rangle \langle u_{-M+1}|e^{iG\hat{x}}|u_M\rangle, \quad (1)$$

where $G = 2\pi/a$ and the inner product is defined in the unit cell [24]. It is normalized to be unity as $\lim_{M \rightarrow \infty} W = \exp(i\theta_{\text{Zak}})$, where θ_{Zak} is simply the Zak phase [25]. The Zak phase specifies a spatial displacement of the localized Wannier orbits that are composed only of the eigenmodes in the n th energy band [24]. In electronic systems, the Zak phase corresponds to surface charge, which can take a fractional value [26–29].

Now, let us translate continuously the one-dimensional periodic potential by ξa ($0 \leq \xi \leq 1$) relative to a fixed frame of the unit cell. The spatial translation changes the potential configuration from U_0 to U_ξ inside the fixed

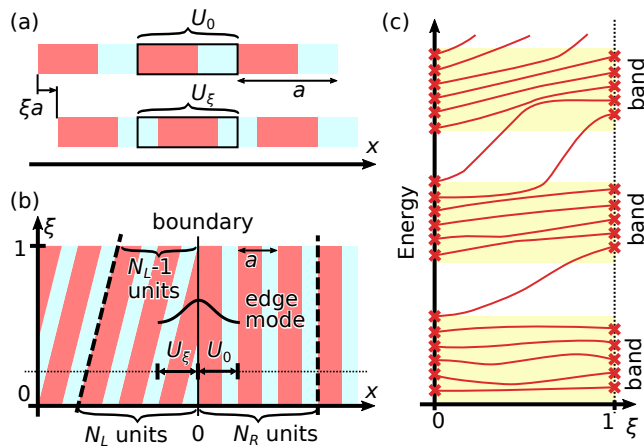


FIG. 1. (a) One-dimensional continuous medium with a periodic potential (upper) and the identical system with spatial translation by ξa (lower). (b) Spatial boundary between the two identical periodic systems with different translations. The Born-von-Karman (BvK) boundary condition is imposed, where the two dashed lines are identified with each other. (c) Eigenenergies of the entire system with the BvK boundary condition are schematically plotted as a function of the translational parameter ξ .

cell [see Fig. 1(a)]. When ξ changes from 0 to 1, the localized Wannier orbit is continuously translated by the periodic length a . Thus, it works like a classical screw pump [30]. Being identical to the displacement of the Wannier orbit with the unit-cell length (apart from a factor $2\pi/a$), the Zak phase also continuously increases by 2π under the translation: $\int_0^1 d\xi \partial_\xi \theta_{\text{Zak}} = 2\pi$. The phase winding counts the Chern integer, which represents the topological characteristics of a fiber bundle on the (k, ξ) plane [24, 31]. In this Letter, ξ is regarded as a variable independent of other variables. Nonetheless, one could consider a continuous change of ξ as a function of time t . In particular, an adiabatic change of $\xi = \xi(t)$ from 0 to 1 in t suppresses interband transitions and is referred to as Thouless pumping [32].

The 2π phase winding in the Zak phase under the translation leads to a series of nontrivial localized states in a spatial boundary between two identical one-dimensional periodic systems with different translations ξ . To see this, let us consider a periodic arrangement of unit cells with U_ξ in a region of $x < 0$ and another periodic arrangement of unit cells with U_0 in the other region of $x \geq 0$. The translation parameter ξ and spatial coordinate x subtend an extended two-dimensional space, as shown in Fig. 1(b). When ξ changes from 0 to 1, the Zak phase in the former bulk region ($x < 0$) winds up the 2π phase. Meanwhile, the Zak phase in the latter bulk region ($x \geq 0$) remains unchanged. Accordingly, the bulk-edge correspondence [24, 31, 32] suggests the existence of zero-dimensional edge states at the boundary region ($x = 0$), whose eigenenergies have “chiral”

dispersions within a bulk band gap as a function of the translational parameter ξ [Fig. 1(c)]. Moreover, as the Zak phase for any bulk band in the region of $x < 0$ acquires the same 2π phase winding during the translation, the number of the chiral dispersions between the n th and $(n+1)$ th bulk bands are expected to be n [Fig. 1(c)].

To prove this bulk-edge correspondence in the translational deformation rigorously, let us impose the following Born-von-Karman (BvK) boundary condition on a finite system [Fig. 1(b)]. Suppose that at $\xi = 0$, the entire one-dimensional system is comprised of N_L unit cells in the region of $x < 0$ and N_R unit cells in the region of $x \geq 0$. For general ξ , we identify $x = -N_L a + \xi a$ with $x = N_R a$, such that the lattice periodicity is preserved at $x = N_R a \equiv -N_L a + \xi a$ and it is broken only at $x = 0$. For $\xi = 0$ and $\xi = 1$, the periodicity is completely preserved in the entire system, so that the eigenmodes at $\xi = 0$ and $\xi = 1$ are all spatially extended bulk band states. Under the BvK boundary condition, which discretizes the Brillouin zone, numbers of the bulk modes in each band at $\xi = 0$ and at $\xi = 1$ are given by $N_L + N_R$ and $N_L + N_R - 1$, respectively. Namely, the number of the extended bulk states decreases by one in each band when ξ continuously changes from 0 to 1. As the energy has a lower bound and there is no upper bound on the bulk band index n in continuous media, more than one eigenmode in each bulk band at $\xi = 0$ must move into bulk bands with a higher energy at $\xi = 1$ during the translation of ξ . For example, when one eigenmode in the lowest bulk band at $\xi = 0$ goes to the second lowest bulk band at $\xi = 1$, two eigenmodes in the second lowest bulk band at $\xi = 0$ must go to the third lowest one at $\xi = 1$ [Fig. 1(c)]. This argument inductively dictates that during the translation of ξ , n modes always raise their energies out of the n th bulk energy band and go across the band gap between the n th and $(n+1)$ th bands. An in-gap mode generally has a complex-valued wave number [33]. Accordingly, the n in-gap modes must be spatially localized at $x = 0$, where the lattice periodicity is broken; therefore, they are simply defect modes localized at the boundary. Importantly, the argument so far does not require any symmetry protection for the presence of the in-gap localized states.

Now, we experimentally confirm the theoretical concept by using microstrip photonic crystals. A microstrip is a transmission line composed of a metallic strip separated from a conducting ground plane by a dielectric substrate. Microwaves propagate between the topside metallic strip and the backside ground plane, and the impedance and refractive index of a microstrip are determined by the geometrical parameters.

The first photonic system studied has a binary unit cell, in which the two strips with different widths behave as two different media. As shown schematically in Fig. 2(a), we continuously introduce a defect around the boundary by displacing the left half by ξa while leaving

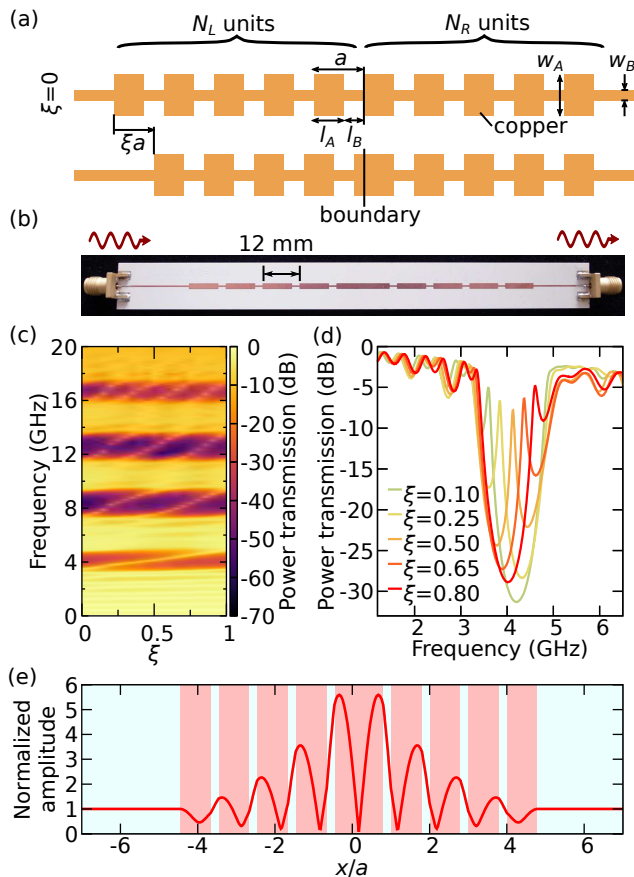


FIG. 2. (a) Schematic top view of binary microstrips at $\xi = 0$ (upper) and at $\xi \neq 0$ (lower). (b) Photograph of a sample with $\xi = 0.35$. The structural parameters are $a = 12$ mm, $l_A/a = 0.8$, $l_B/a = 0.2$, $w_A = 1.8$ mm, $w_B = 0.45$ mm, and $N_L = N_R = 5$. The microstrip is made of a $35 \mu\text{m}$ -thick copper film on a polyphenylene-ether substrate (RISHO CS-3396; thickness 0.56 mm, $\epsilon = 11.3$, $\tan \delta = 0.003$ at 1 GHz), and SMA connectors (GIGALANE PSF-S01-001) are attached to the substrate. The back of the substrate contains a ground plane made of a copper film with the same thickness as the microstrip. (c) Power transmission spectra through the 21 samples from $\xi = 0$ to $\xi = 1$ with the step size of $\Delta\xi = 0.05$. The input power is set to 0 dBm. (d) Power transmission spectra inside the first band gap for several values of ξ . (e) Calculated distribution of the absolute value of the complex electric-field amplitude at 4.22 GHz with $\xi = 0.538$ inside the first band gap. The amplitude is normalized to that of the incident field. Regions of different colors represent different width strips.

the right half unchanged. A photograph of one of the fabricated samples ($\xi = 0.35$) is provided in Fig. 2(b). Using a vector network analyzer (KEYSIGHT 5232A), we measured the power transmission through the samples with ξ from 0 to 1 with a step size of $\Delta\xi = 0.05$. The transmission spectra obtained for these different ξ are summarized in Fig. 2(c). Under 20 GHz, we clearly see five transmission bands, and four band gaps between them. The n th band gap has n boundary modes running between the two neighboring transmission bands, as expected from

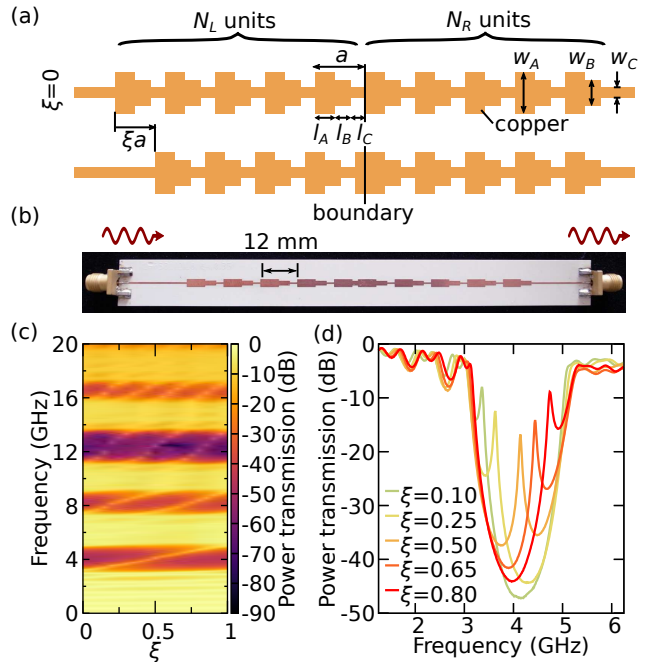


FIG. 3. (a) Schematic top view of ternary microstrips at $\xi = 0$ (upper) and at $\xi \neq 0$ (lower). (b) Photograph of a sample with $\xi = 0.35$. The structural parameters are $l_A/a = 0.5$, $l_B/a = 0.3$, $l_C/a = 0.2$, $w_A = 2.5$ mm, $w_B = 1.5$ mm, and $w_C = 0.45$ mm. The other parameters are the same as those in Fig. 2. (c) Power transmission spectra through the 21 samples from $\xi = 0$ to $\xi = 1$ with a step size of $\Delta\xi = 0.05$. (d) Power transmission spectra inside the first band gap for several values of ξ .

the theory. The qualitative behavior of the transmission spectra can be well captured by a transfer-matrix model calculation [34]. Figure 2(d) shows some of the experimentally obtained power transmission spectra inside the first band gap. The transmission peak decreases and the line width becomes narrower around $\xi = 0.50$. This is because coupling between the incident wave and the boundary mode is reduced at the center of the band gap. In fact, the transfer-matrix model calculation confirms that the localized mode becomes the narrowest at the center of the first band gap [34], as plotted in Fig. 2(e).

The second photonic system studied has three components in the unit cell. The design and photograph of the ternary microstrips are shown in Figs. 3(a) and 3(b), respectively. With three different regions, the unit cell has no spatial inversion symmetry at any ξ . Figures 3(c) and 3(d) illustrate the experimental transmission spectra for 21 samples with different ξ [34]. These transmission spectra confirm that the n localized modes run across the n th transmission gap during the translation of ξ from 0 to 1 . The experimental results clearly demonstrate that inversion symmetry is not essential for the generation of the series of localized states through translational deformation.

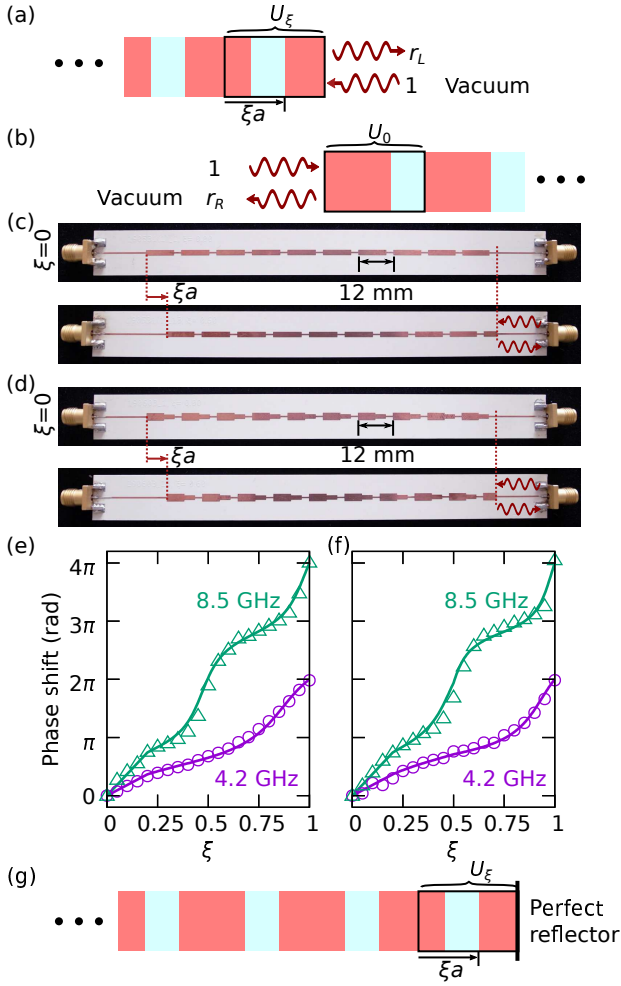


FIG. 4. Definitions of (a) left and (b) right complex reflection amplitudes $r_L(\xi, \omega)$ and $r_R(\omega)$, respectively. Photograph of (c) binary and (d) ternary samples ($\xi = 0$ and 0.60) to measure $r_L(\xi, \omega)$. The parameters are the same as those in Figs. 2 and 3. Topological winding of $\arg[r_L(\xi, \omega_0)] - \arg[r_L(0, \omega_0)]$ as a function of ξ for (e) binary and (f) ternary samples. Here, ω_0 is set to $2\pi \times 4.20$ GHz and $2\pi \times 8.50$ GHz inside the first band gap (circles) and second band gap (triangles), respectively. A microwave is injected from the right connector; meanwhile, the left connector is connected to another port of the network analyzer through a cable. The theoretical curves for the semi-infinite systems are plotted with the experimentally obtained points. Note that we use the convention of $\arg e^{j\theta} = \theta$ for $j = -i$. (g) One-dimensional photonic crystal terminated by a perfect reflector.

Next, we establish the physical origin of the localized states in terms of phase winding of the complex reflection amplitude. To this end, we divide the deformed crystal into two halves. Namely, the left region with U_ξ is now terminated at its right end by a vacuum region, while the right region with U_0 is terminated by the same vacuum region at its left end [Figs. 4(a) and 4(b)]. Photonic properties of each semi-infinite region are characterized by the complex reflection amplitude r or a rela-

tive surface impedance $Z^{(s)} \equiv (1+r)/(1-r)$ at the respective termination. The topological characteristics of localized states are encoded between the complex reflection amplitudes at both terminations $r_L(\xi, \omega)$ and $r_R(\omega)$ with an angular frequency ω . Specifically, a condition for eigenmodes localized at the original defect is nothing but the resonance condition across the two terminations: $Z_L^{(s)}(\xi, \omega) + Z_R^{(s)}(\omega) = 0$. The resonance condition can also be written as $r_L(\xi, \omega)r_R(\omega) = 1$. When ω remains inside the band gap between the n th and $(n+1)$ th bulk bands, both the semi-infinite regions behave as perfect reflectors: $|r_R(\omega)| = |r_L(\xi, \omega)| = 1$ under assumption of no dissipation. Thus, the condition shows that the phase of $r_L(\xi, \omega)$ must wind up by $2\pi n$ during the translation from $\xi = 0$ to $\xi = 1$, because the n boundary modes move across the angular frequency ω in the gap. The direction of the winding is determined by Foster's theorem [34, 35].

The $2\pi n$ phase winding of the reflection is considered as the physical origin of the localized states. To confirm this phase winding experimentally, we fabricated samples composed only of the left-half parts with different ξ , as in Figs. 4(c) and 4(d). Figures 4(e) and 4(f) show measured phases of the reflected waves of samples with different ξ (relative to the measured phase at $\xi = 0$). The experimental data points agree well with the theoretical curves obtained from the transfer-matrix model calculations for the semi-infinite systems [34]. The results clearly demonstrate the presence of phase winding of the reflection amplitude, regardless of the unit-cell symmetry.

The phase winding of the reflection provides a unified perspective on both Tamm and Shockley states, which are often separately attributed to a perturbed surface potential and band inversion, respectively [1, 2, 8]. To this end, we consider that the left region with U_ξ is terminated by a perfect reflector at the right end as shown in Fig. 4(g). Given $|r_R(\omega)| = 1$ for those ω in the n th transmission gap of the left part, the $2\pi n$ phase winding of $r_L(\xi, \omega)$ during the translation of ξ from 0 to 1 always guarantees the emergence of n localized eigenmodes at the termination, irrespective of the details of the reflector on the right side. This holds true for any reflector with ξ -independent perturbations, provided the perturbations maintain the perfect-reflection condition. Such perturbations include a delta-function-like surface perturbation, the existence of which distinguishes Tamm states from Shockley states, as discussed in Ref. [2]. In this sense, our proposed mechanism provides a comprehensive viewpoint for both Tamm and Shockley states.

In summary, we demonstrated a scenario that produces localized states through translational deformations analogous to classical screw pumping. The mechanism is not restricted to a specific physical system; rather, it is universal for any waves. Localized states in a system, even in the absence of sublattice or inversion symmetry, are now interpreted as topological boundary modes. The termination at the spatial boundary is understood as an engi-

neered degree of freedom and can be used for tuning the spatial localization of the boundary mode.

The authors thank K. Usami, A. Noguchi, and M. W. Takeda for their fruitful discussions, and J. Koenig for his careful reading of the manuscript. This work was supported by JSPS KAKENHI (Grant No. 17K17777) and by the JST ERATO project (Grant No. JPM-JER1601). R. S. was supported by National Basic Research Programs of China (973 program Grants No. 2014CB920901 and No. 2015CB921104) and National Natural Science Foundation of China (Grants No. 2017A040215).

* nakata@ee.es.osaka-u.ac.jp

- [1] I. Tamm, Über eine mögliche art der elektronenbindung an kristalloberflächen, *Phys. Z. Sowjetunion* **1**, 733 (1932).
- [2] W. Shockley, On the surface states associated with a periodic potential, *Phys. Rev.* **56**, 317 (1939).
- [3] H. M. James, Electronic states in perturbed periodic systems, *Phys. Rev.* **76**, 1611 (1949).
- [4] D. S. Saxon and R. A. Hunter, Some electronic properties of a one-dimensional crystal model, *Philips Res. Rep.* **4**, 81 (1949).
- [5] H. Ohno, E. E. Mendez, J. A. Brum, J. M. Hong, F. Agulló-Rueda, L. L. Chang, and L. Esaki, Observation of “Tamm states” in Superlattices, *Phys. Rev. Lett.* **64**, 2555 (1990).
- [6] P. Yeh, A. Yariv, and A. Y. Cho, Optical surface waves in periodic layered media, *Appl. Phys. Lett.* **32**, 104 (1978).
- [7] T. Goto, A. V. Dorofeenko, A. M. Merzlikin, A. V. Baryshev, A. P. Vinogradov, M. Inoue, A. A. Lisyansky, and A. B. Granovsky, Optical Tamm States in One-Dimensional Magnetophotonic Structures, *Phys. Rev. Lett.* **101**, 113902 (2008).
- [8] A. P. Vinogradov, A. V. Dorofeenko, A. M. Merzlikin, and A. A. Lisyansky, Surface states in photonic crystals, *Phys. Usp.* **53**, 243 (2010).
- [9] H. Kitahara, T. Kawaguchi, J. Miyashita, and M. Wada Takeda, Impurity mode in microstrip line photonic crystal in millimeter wave region, *J. Phys. Soc. Jpn.* **72**, 951 (2003).
- [10] H. Kitahara, T. Kawaguchi, J. Miyashita, R. Shimada, and M. Wada Takeda, Strongly localized singular Bloch modes created in dual-periodic microstrip lines, *J. Phys. Soc. Jpn.* **73**, 296 (2004).
- [11] J. Guo, Y. Sun, Y. Zhang, H. Li, H. Jiang, and H. Chen, Experimental investigation of interface states in photonic crystal heterostructures, *Phys. Rev. E* **78**, 026607 (2008).
- [12] M. E. Sasin, R. P. Seisyan, M. A. Kalitchevski, S. Brand, R. A. Abram, J. M. Chamberlain, A. Y. Egorov, A. P. Vasil'ev, V. S. Mikhlin, and A. V. Kavokin, Tamm plasmon polaritons: Slow and spatially compact light, *Appl. Phys. Lett.* **92**, 251112 (2008).
- [13] G. C. Dyer, G. R. Aizin, S. J. Allen, A. D. Grine, D. Bethke, J. L. Reno, and E. A. Shaner, Induced transparency by coupling of Tamm and defect states in tunable terahertz plasmonic crystals, *Nat. Photonics* **7**, 925 (2013).
- [14] M. Xiao, G. Ma, Z. Yang, P. Sheng, Z. Q. Zhang, and C. T. Chan, Geometric phase and band inversion in periodic acoustic systems, *Nat. Phys.* **11**, 240 (2015).
- [15] C. L. Kane and E. J. Mele, Z_2 Topological Order and the Quantum Spin Hall Effect, *Phys. Rev. Lett.* **95**, 146802 (2005).
- [16] L. Fu, C. L. Kane, and E. J. Mele, Topological Insulators in Three Dimensions, *Phys. Rev. Lett.* **98**, 106803 (2007).
- [17] M. König, S. Wiedmann, C. Brüne, A. Roth, H. Buhmann, L. W. Molenkamp, X.-L. Qi, and S.-C. Zhang, Quantum spin Hall insulator state in HgTe quantum wells, *Science* **318**, 766 (2007).
- [18] Y. L. Chen, J. G. Analytis, J.-H. Chu, Z. K. Liu, S.-K. Mo, X. L. Qi, H. J. Zhang, D. H. Lu, X. Dai, Z. Fang, S. C. Zhang, I. R. Fisher, Z. Hussain, and Z.-X. Shen, Experimental realization of a three-dimensional topological insulator, Bi_2Te_3 , *Science* **325**, 178 (2009).
- [19] A. P. Schnyder, S. Ryu, A. Furusaki, and A. W. W. Ludwig, Classification of topological insulators and superconductors in three spatial dimensions, *Phys. Rev. B* **78**, 195125 (2008).
- [20] W. P. Su, J. R. Schrieffer, and A. J. Heeger, Solitons in Polyacetylene, *Phys. Rev. Lett.* **42**, 1698 (1979).
- [21] W. P. Su, J. R. Schrieffer, and A. J. Heeger, Soliton excitations in polyacetylene, *Phys. Rev. B* **22**, 2099 (1980).
- [22] M. Xiao, Z. Q. Zhang, and C. T. Chan, Surface Impedance and Bulk Band Geometric Phases in One-Dimensional Systems, *Phys. Rev. X* **4**, 021017 (2014).
- [23] N. W. Ashcroft and N. D. Mermin, *Solid State Physics* (Holt, Rinehart and Winston, New York, 1976).
- [24] D. Vanderbilt, *Berry Phases in Electronic Structure Theory: Electric Polarization, Orbital Magnetization and Topological Insulators* (Cambridge University Press, Cambridge, England, 2018).
- [25] J. Zak, Berry's Phase for Energy Bands in Solids, *Phys. Rev. Lett.* **62**, 2747 (1989).
- [26] D. Vanderbilt and R. D. King-Smith, Electric polarization as a bulk quantity and its relation to surface charge, *Phys. Rev. B* **48**, 4442 (1993).
- [27] S. Gangadharaiah, L. Trifunovic, and D. Loss, Localized End States in Density Modulated Quantum Wires and Rings, *Phys. Rev. Lett.* **108**, 136803 (2012).
- [28] J.-H. Park, G. Yang, J. Klinovaja, P. Stano, and D. Loss, Fractional boundary charges in quantum dot arrays with density modulation, *Phys. Rev. B* **94**, 075416 (2016).
- [29] M. Thakurathi, J. Klinovaja, and D. Loss, From fractional boundary charges to quantized Hall conductance, *Phys. Rev. B* **98**, 245404 (2018).
- [30] T. Ozawa, H. M. Price, A. Amo, N. Goldman, M. Hafezi, L. Lu, M. C. Rechtsman, D. Schuster, J. Simon, O. Zilberberg, and I. Carusotto, Topological photonics, *Rev. Mod. Phys.* **91**, 015006 (2019).
- [31] J. K. Asbóth, L. Oroszlány, and A. Pályi, *A Short Course on Topological Insulators* (Springer, Cham, Switzerland, 2016).
- [32] D. J. Thouless, Quantization of particle transport, *Phys. Rev. B* **27**, 6083 (1983).
- [33] A. A. Cottley, Floquet's theorem and band theory in one dimension, *Am. J. Phys.* **39**, 1235 (1971).
- [34] See Supplemental Material for detailed information of the transfer-matrix method, comparison of theoretical

and experimental transmission data, characterization of localized states, full reflection properties of the semi-infinite systems, and winding direction of complex reflection amplitudes.

- [35] R. E. Collin, *Foundations for Microwave Engineering*, 2nd ed. (McGraw-Hill, New York, 1996).
- [36] B. E. A. Saleh and M. C. Teich, *Fundamentals of Photonics*, 2nd ed. (John Wiley & Sons, Inc., Hoboken, New Jersey, 2007).
- [37] E. Hammerstad and O. Jensen, Accurate models for microstrip computer-aided design, in *1980 IEEE MTT-S Int. Microwave Symp. Dig.* (IEEE, Washington, 1980) pp. 407–409.

Supplemental Material for “Topological Boundary Modes from Translational Deformations”

Transfer-matrix method

Here, we explain a calculation technique known as the transfer-matrix method for one-dimensional scalar wave propagation [35, 36]. Consider a two-port system with complex amplitudes a_1 , a_2 , b_1 , and b_2 of incoming and outgoing signals, as shown in Fig. S1. The scattering property of the system is modeled by a 2×2 scattering matrix S as

$$\begin{bmatrix} b_1 \\ b_2 \end{bmatrix} = S \begin{bmatrix} a_1 \\ a_2 \end{bmatrix}. \quad (\text{S1})$$

To connect the systems, we also introduce a 2×2 transfer matrix T as

$$\begin{bmatrix} a_1 \\ b_1 \end{bmatrix} = T \begin{bmatrix} b_2 \\ a_2 \end{bmatrix}. \quad (\text{S2})$$

By multiplying these transmission matrices, we obtain a total transmission matrix. The scattering and transfer matrices are related as follows: $S_{11} = T_{21}/T_{11}$, $S_{12} = T_{22} - T_{21}T_{12}/T_{11}$, $S_{21} = 1/T_{11}$, and $S_{22} = -T_{12}/T_{11}$. Conversely, we have $T_{11} = 1/S_{21}$, $T_{12} = -S_{22}/S_{21}$, $T_{21} = S_{11}/S_{21}$, and $T_{22} = S_{12} - S_{11}S_{22}/S_{21}$.

At a specific point in a one-dimensional photonic system, we can represent an electric field with an angular frequency ω as

$$\frac{E}{\sqrt{Z_0 Z_X}} = \frac{1}{\sqrt{2}}(a + b) \exp(j\omega t) + \text{c.c.}, \quad (\text{S3})$$

where we have an incoming complex amplitude a , outgoing complex amplitude b , vacuum impedance Z_0 , and relative impedance $Z_X = \sqrt{\mu_X/\epsilon_X}$ with relative permittivity ϵ_X and relative permeability μ_X at the point in a material X . Here, c.c. represents the complex conjugate of the preceding term. Note that we use the imaginary unit $j = -i$ for a photonic system, and Im represents the coefficient of the imaginary part, which is represented by j . At the boundary between two regions with material X (left) and Y (right), we have the following scattering matrix:

$$S_{XY}^{(b)} = \frac{1}{Z_X + Z_Y} \begin{bmatrix} Z_Y - Z_X & 2\sqrt{Z_X Z_Y} \\ 2\sqrt{Z_X Z_Y} & Z_X - Z_Y \end{bmatrix}. \quad (\text{S4})$$

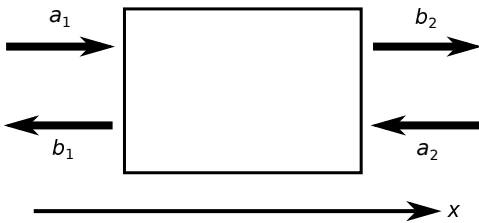


FIG. S1. Model of two-port system.

Correspondingly, we have $T_{XY}^{(b)}$ as the transfer matrix for $S_{XY}^{(b)}$. For free propagation across a length l in X , we have the following transfer matrix:

$$T_X^{(f)}(\omega) = \begin{bmatrix} \exp(jk_X l) & 0 \\ 0 & \exp(-jk_X l) \end{bmatrix}, \quad (\text{S5})$$

with wave number $k_X = \omega/c_X$ and speed of light c_X in X . By using a refractive index $n_X = \sqrt{\epsilon_X \mu_X}$ in X , c_X is written as c_0/n_X , with the speed of light c_0 in a vacuum.

Now, we consider a unit cell of a photonic crystal with length l_m of material X_m from left to right ($m = 1, 2, \dots, L$). The transfer matrix of the unit cell is defined as

$$T^{\text{unit}}(\omega) = T_{X_L X_1}^{(b)} T_{X_1}^{(f)}(\omega) \prod_{m=2}^L T_{X_{m-1} X_m}^{(b)} T_{X_m}^{(f)}(\omega). \quad (\text{S6})$$

Eigenvalues of $T^{\text{unit}}(\omega)$ are given by $\exp(jka)$ with the complex Bloch wave number k and the unit-cell length $a = \sum_m l_m$. From an eigenvector $\mathbf{v} = [v_1 \ v_2]^T$ with $\text{Im}(k) > 0$ (decaying to left) for $T^{\text{unit}}(\omega)$ inside a band gap, we can calculate $r_L = w_1/w_2$ by using $\mathbf{w} = [w_1 \ w_2]^T = (T_{X_L V}^{(b)})^{-1} \mathbf{v}$ with a vacuum V for the model shown in Fig. 4(a) of the main text. The theoretical curves in Figs. 4(e) and 4(f) are calculated by this method, while we regard the wave-launching region as a “vacuum.”

To obtain the power transmission, we calculate a total transmission matrix T^{tot} for the entire system, and then convert it to the scattering matrix S^{tot} . Then, we have the power transmission $|S_{21}^{\text{tot}}|^2$ for an incident wave from the left. Multiplying a series of transfer matrices to $\mathbf{v}_{\text{out}} = [S_{21}^{\text{tot}} \ 0]^T$, we obtain the electric-field distribution.

Comparison of theoretical and experimental transmission data

Here, we calculate transmission spectra of the binary and ternary photonic crystals [Figs. S2(a) and S3(a), respectively] and compare the results with the experimental data. The quasistatic refractive indices and impedances of the microstrips are calculated from formula derived by E. Hammerstad and O. Jensen [37]. The calculated photonic bulk bands are shown in Figs. S2(b) and S3(b), and the expected transmission spectra are indicated in Figs. S2(c) and S3(c). We can see that the bulk bands in Figs. S2(b) and S3(b) correspond to the high transmission regions in Figs. S2(c) and S3(c), respectively. The experimental transmission spectra are also shown in Figs. S2(d) and S3(d). The experimental transmission power is not as high as that calculated in the

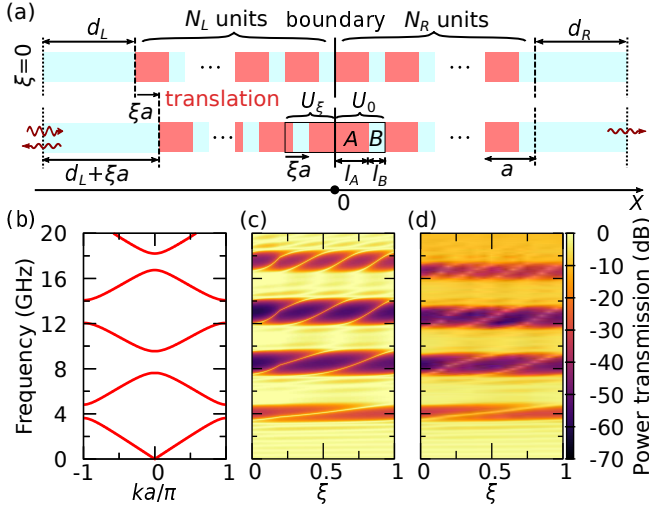


FIG. S2. (a) Theoretical model for the binary photonic crystals shown in Fig. 2 of the main text. Starting from a system without a defect (upper), we translate the left region ($x < 0$) by ξa (lower). The structural parameters are $a = 12$ mm, $l_A/a = 0.8$, $l_B/a = 0.2$, with $N_L = N_R = 5$. The regions of A and B have $(n_A, Z_A) = (2.92, 22.6 \Omega)$ and $(n_B, Z_B) = (2.73, 49.6 \Omega)$, respectively. Waves enter from the left. The two extra regions of B are attached to the system with $d_L/a = d_R/a = 2$. (b) Real band structure of the system without a defect. (c) Theoretically and (d) experimentally obtained transmission spectra.

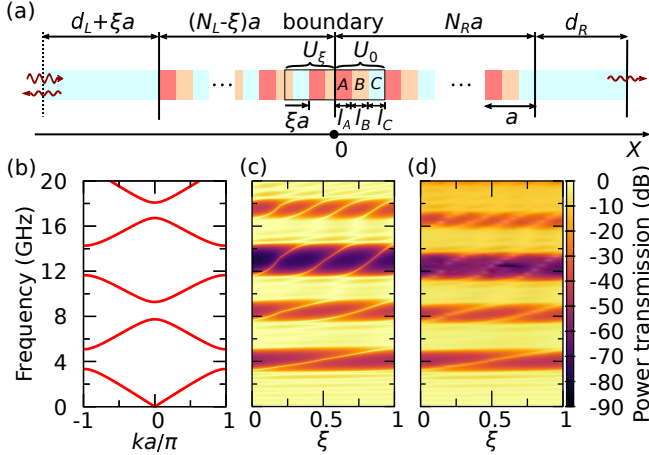


FIG. S3. (a) Theoretical model for the ternary photonic crystals shown in Fig. 3 of the main text. The left region ($x < 0$) is translated by ξa . The structural parameters are $a = 12$ mm, $l_A/a = 0.5$, $l_B/a = 0.3$, and $l_C/a = 0.2$ with $N_L = N_R = 5$. The regions of A, B, and C have $(n_A, Z_A) = (2.97, 17.8 \Omega)$, $(n_B, Z_B) = (2.89, 25.6 \Omega)$, and $(n_C, Z_C) = (2.73, 49.6 \Omega)$, respectively. Waves enter from the left. The two extra regions of C are attached to the system with $d_L/a = d_R/a = 2$. (b) Real band structure of the system without a defect. (c) Theoretically and (d) experimentally obtained transmission spectra.

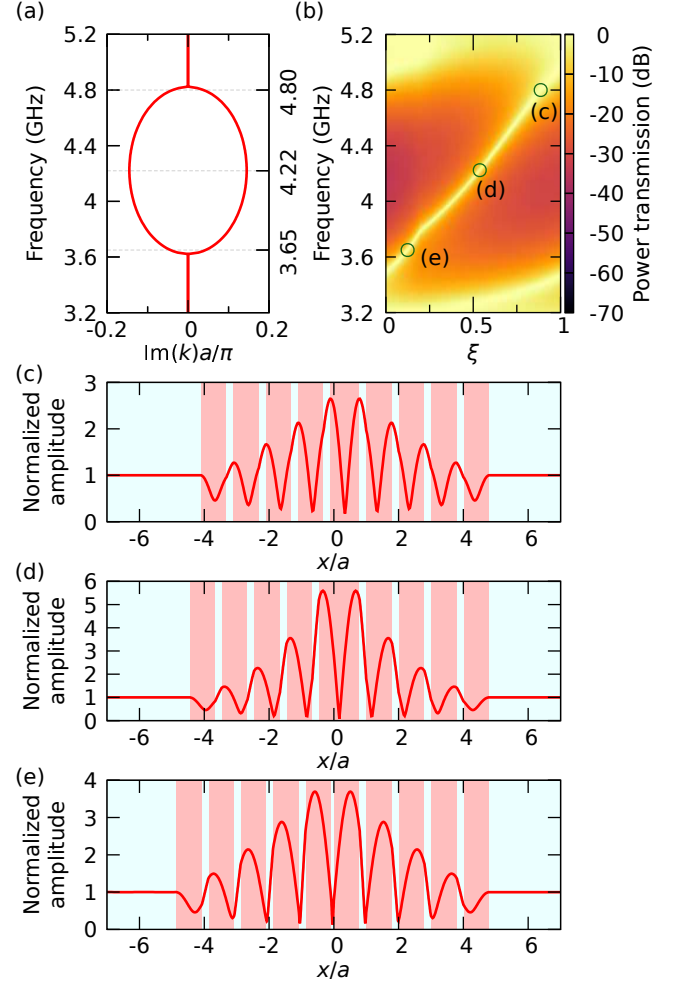


FIG. S4. Localization in the first band gap of the binary system of Fig. S2 with $N_L = N_R = 5$. (a) Imaginary part of the complex wave number for the system without a defect. (b) Power transmission spectra, indicating an enlarged view of Fig. S2(c). (c)–(e) Distribution of the absolute value of the complex electric-field amplitude for $(\xi, \omega) = (0.887, 2\pi \times 4.8$ GHz), $(0.538, 2\pi \times 4.22$ GHz), and $(0.124, 2\pi \times 3.65$ GHz), respectively. These points are also indicated in (a) by dashed lines and in (b) by circles. The field values are normalized by the incident-wave amplitude.

higher frequency region. This is because losses (dielectric, metallic, or radiative) are not included in the model. The calculated transmission-band frequencies show good agreement with the experimental data, especially in the lower frequency region. Discrepancies in the higher frequency region can be attributed to the effect of dispersion in the microstrips, which is not taken into account in the model calculation. Nonetheless, the topological behaviors of the localized states that migrate across the transmission gaps agree very well between theory and experiment in the entire frequency region.

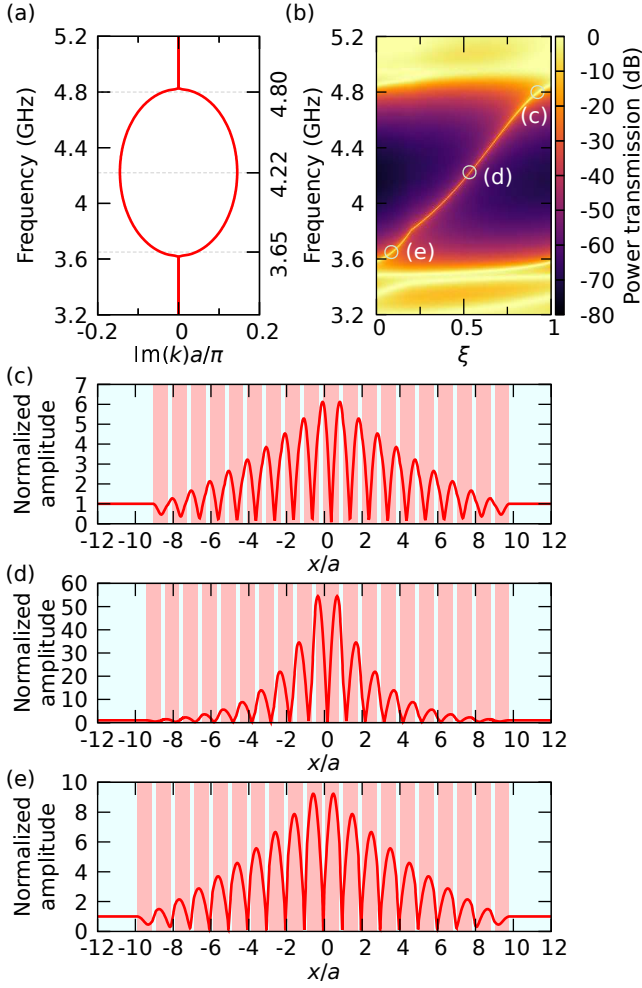


FIG. S5. Localization in the first band gap of the binary system with $N_L = N_R = 10$. The other parameters are the same as those in Fig. S2. (a) Imaginary part of the complex wave number for the system without a defect. (b) Calculated power transmission spectra. (c)–(e) Distribution of the absolute value of the complex electric-field amplitude for $(\xi, \omega) = (0.923, 2\pi \times 4.80 \text{ GHz})$, $(0.533, 2\pi \times 4.22 \text{ GHz})$, and $(0.0855, 2\pi \times 3.65 \text{ GHz})$. These points are also indicated in (a) by dashed lines and in (b) by circles. The field values are normalized by the incident-wave amplitude.

Characterization of localized states

In this section, we characterize the field distribution of the localized states, based on the theoretical-model calculations. First, we analyze the binary photonic crystals. Generally, we have complex wave numbers inside band gaps. Figure S4(a) shows the imaginary part of the complex wave number inside the first band gap for the model. Near the center of the band gap, the imaginary part is maximized. Figure S4(b) shows the power transmission, which is enlarged from Fig. S2(c). To see the variation of the distribution, we took three points along the boundary-mode dispersion depicted as

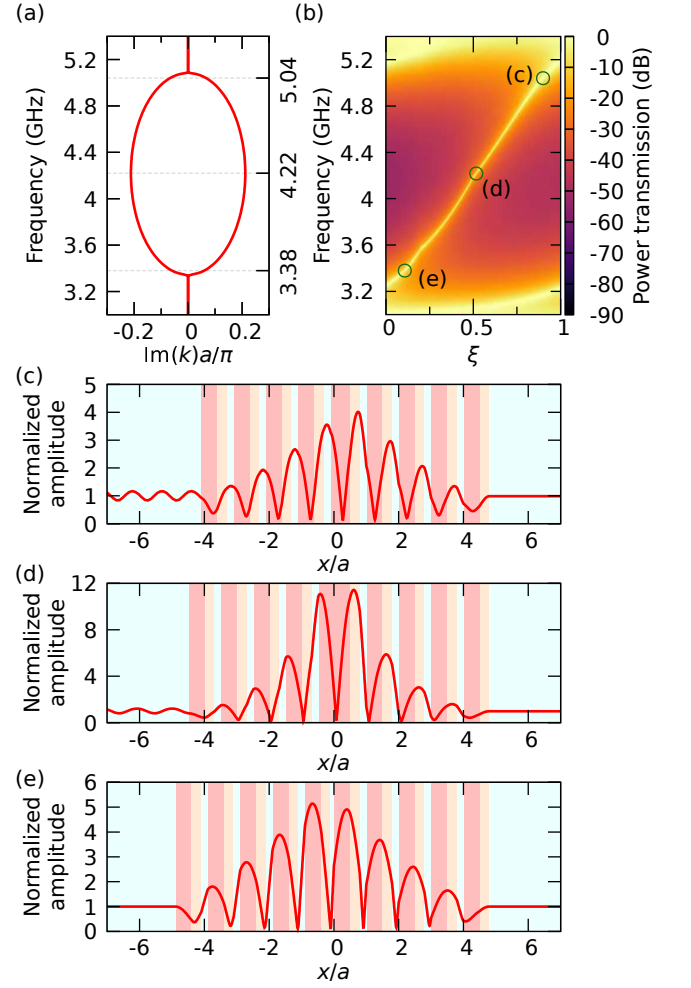


FIG. S6. Localization in the first band gap of the ternary system of Fig. S3 with $N_L = N_R = 5$. (a) Imaginary part of the complex wave number for the system without a defect. (b) Power transmission spectra, indicating an enlarged view of Fig. S3(c). (c)–(e) Distribution of the absolute value of the complex electric-field amplitude for $(\xi, \omega) = (0.899, 2\pi \times 5.04 \text{ GHz})$, $(0.517, 2\pi \times 4.22 \text{ GHz})$, and $(0.107, 2\pi \times 3.38 \text{ GHz})$, respectively. These points are also indicated in (a) by dashed lines and in (b) by circles. The field values are normalized by the incident-wave amplitude.

circles in Fig. S4(b). The corresponding field distributions are plotted in Figs. S4(c)–(e). As we expected from Fig. S4(a), localization is the narrowest in the center of the band gap. To observe the localization tuning more clearly, we increase $N_L = N_R = 10$ from $N_L = N_R = 5$ while the other parameters are left unchanged. The calculated results are summarized in Fig. S5. A comparison of Figs. S5(c)–(e) clearly shows the realization of the narrowest localization in the band-gap center. Thus, we can tune localization by altering ξ , i.e., the termination. The narrowest localization decreases the coupling to the incident wave, and the radiative loss is reduced more effectively. For completeness, we also show data for

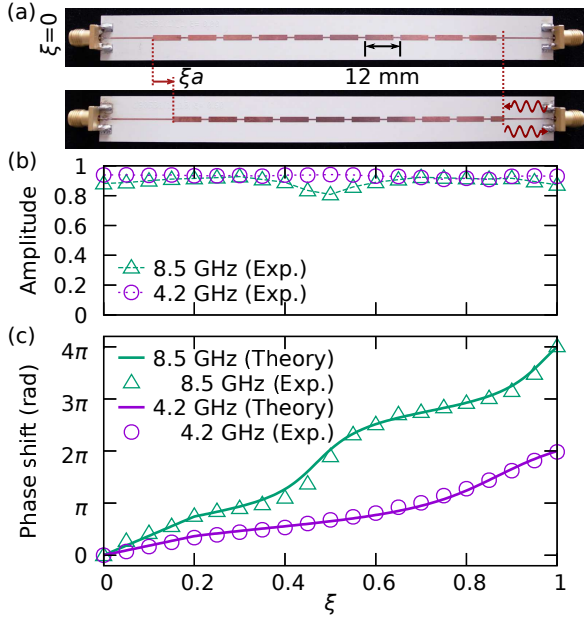


FIG. S7. (a) Photograph of binary samples ($\xi = 0$ and 0.60) to measure $r_L(\xi, \omega)$. (b) Reflection amplitude $|r_L(\xi, \omega_0)|$ and (c) phase shift $\arg[r_L(\xi, \omega_0)] - \arg[r_L(0, \omega_0)]$ as a function of ξ . Here, ω_0 is set to $2\pi \times 4.20$ GHz and $2\pi \times 8.50$ GHz inside the first and second band gaps, respectively. A microwave is injected from the right connector; meanwhile, the left connector is connected to another port of the network analyzer through a cable. The theoretical curves for the semi-infinite system are plotted in (c) with the experimentally obtained points.

the ternary photonic crystals in Fig. S6. The inversion-symmetry breaking leads to nonsymmetric field distributions in Figs. S6(c)–(e).

Full reflection properties of the half systems

Here, we provide reflection-amplitude data for the half photonic crystals, in addition to the phase data of Figs. 4(e) and 4(f). Figures S7 and S8 show the complete data of reflection coefficients for the binary and ternary halves, respectively. The reflection amplitude $|r_L(\xi, \omega_0)|$ should be unity in the theoretical models; however, it is degraded by the finite dissipation in the experiments. Slight changes in the reflection amplitudes with respect to ξ are observed in Figs. S7(b) and S8(b). This can be attributed to the resonance, which is caused by a change in the length of the first strip located near the reflection boundary.

Winding direction of complex reflection amplitudes

Based on Foster's theorem, let us determine the rotation direction of $r_L(\xi, \omega_0)$ from $\xi = 0$ to $\xi = 1$ for fixed

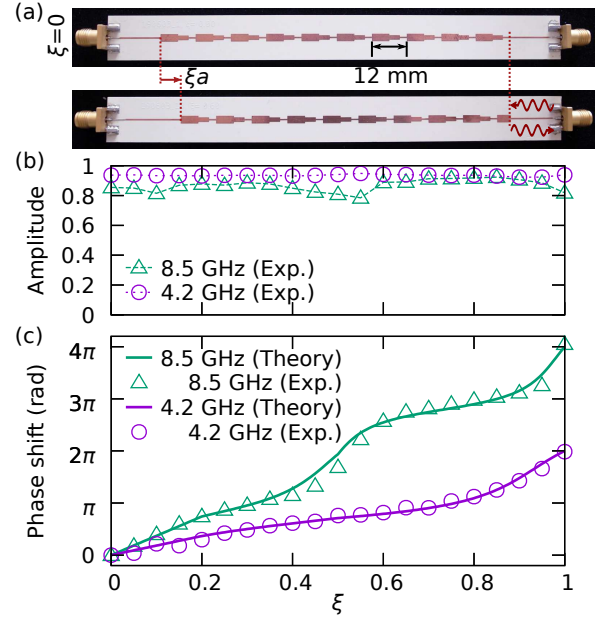


FIG. S8. (a) Photograph of ternary samples ($\xi = 0$ and 0.60) to measure $r_L(\xi, \omega)$. (b) Reflection amplitude $|r_L(\xi, \omega_0)|$ and (c) phase shift $\arg[r_L(\xi, \omega_0)] - \arg[r_L(0, \omega_0)]$ as a function of ξ . Here, ω_0 is set to $2\pi \times 4.20$ GHz and $2\pi \times 8.50$ GHz inside the first and second band gaps, respectively. A microwave is injected from the right connector; meanwhile, the left connector is connected to another port of the network analyzer through a cable. The theoretical curves for the semi-infinite system are plotted in (c) with the experimentally obtained points.

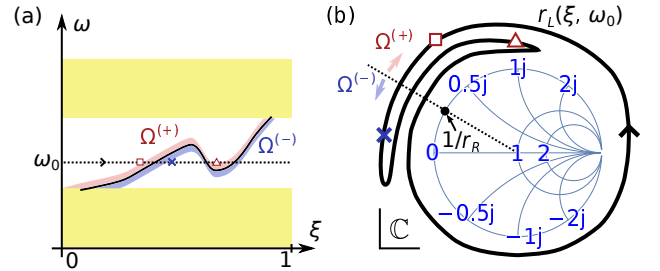


FIG. S9. (a) Possible situation for an boundary-mode transition for the first band gap. (b) Corresponding trajectory of $r_L(\xi, \omega_0)$ from $\xi = 0$ to 1 with the Smith chart, while fixing $\omega = \omega_0$.

ω_0 inside a band gap. In this section, we focus on the band gap between the n th and $(n+1)$ th bands. Thus, the total number of migrating localized modes from the n th to $(n+1)$ th bands is n .

The eigenfrequencies of localized modes inside the band gap are written as $\omega = \omega_m(\xi)$, which are determined by $r_L(\xi, \omega)r_R(\omega) = 1$. Here, we consider the following regions with a small $\Delta\omega > 0$: $\Omega^{(+)} = \bigcup_m \Omega_m^{(+)}$ and $\Omega^{(-)} = \bigcup_m \Omega_m^{(-)}$, where $\Omega_m^{(+)} = \{(\xi, \omega) | \xi \in [0, 1], \omega_m(\xi) < \omega < \omega_m(\xi) + \Delta\omega\}$ and $\Omega_m^{(-)} = \{(\xi, \omega) | \xi \in [0, 1], \omega_m(\xi) - \Delta\omega <$

$\omega < \omega_m(\xi)$ }. A possible situation for $n = 1$ is graphically shown in Fig. S9. Foster's reactance theorem can be applied, provided that the system is passive [35]. Then, $r_L(\xi, \omega)r_R(\omega)$ must monotonically rotate clockwise in the complex plane when we increase ω . Therefore, we have $\arg r_L < -\arg r_R$ and $\arg r_L > -\arg r_R$ for $\Omega^{(+)}$ and $\Omega^{(-)}$, respectively.

Now, consider $r_L(\xi, \omega_0)$, with a specified ω_0 inside the band gap. We assume there is no degeneracy of localized states at $\omega = \omega_0$. In other words, we always have $p = q$ if $\omega_p(\xi) = \omega_q(\xi) = \omega_0$. By changing ξ from 0 to 1 along

$\omega = \omega_0$, the total number of transitions from $\Omega^{(+)}$ to $\Omega^{(-)}$ must be n owing to the bulk-edge correspondence. In the Smith chart, $\Omega^{(+)} \rightarrow \Omega^{(-)}$ corresponds to the situation that r_L crosses over $[r_R(\omega_0)]^{-1}$ in an anti-clockwise manner. Similarly, $\Omega^{(-)} \rightarrow \Omega^{(+)}$ represents clockwise crossing. Then, the winding number in the Smith chart must be n in an anti-clockwise manner with changing ξ from 0 to 1 because the trajectory is continuous. If there is an accidental degeneracy, we may consider an angular frequency ω'_0 that is slightly displaced from ω_0 to avoid this degeneracy. Owing to the continuity, the winding number at ω_0 must be the same as that at ω'_0 .